A Two-Dimensional Type I Superionic Conductor

Alexander J. E. Rettie[1,2,*], Jingxuan Ding,[3] Xiuquan Zhou,[1] Michael J. Johnson,[2] Christos D. Malliakas,[4] Naresh C. Osti,[5] Duck Young Chung[1], Raymond Osborn,[1] Olivier Delaire,[3] Stephan Rosenkranz,[1,*] Mercouri G. Kanatzidis[1,4,*]

1. Materials Science Division, Argonne National Laboratory, Lemont, IL, 60439, USA
2. Electrochemical Innovation Lab, Department of Chemical Engineering, University College London, Bloomsbury, London, WC1E 6BT, UK
3. Departments of Mechanical Engineering, Materials Science and Physics, Duke University, Durham, NC, 27708, USA
4. Department of Chemistry, Northwestern University, Evanston, IL, 60208, USA
5. Neutron Scattering Division, Oak Ridge National Laboratory, Oak Ridge, TN, 37831, USA

* Correspondence to: a.rettie@ucl.ac.uk, srosenkranz@anl.gov, m-kanatzidis@northwestern.edu

Abstract

Superionic conductors (SICs) possess liquid-like ionic diffusivity in the solid state, finding wide applicability from electrolytes in energy storage to materials for thermoelectric energy conversion. Type I SICs (e.g., AgI, Ag_2Se, etc.) are defined by an abrupt transition to the superionic state and have so far been found exclusively in three-dimensional crystal structures. Here, we reveal a two-dimensional type I SIC, α-KAg_3Se_2 by scattering techniques and complementary simulations. Quasi-elastic neutron scattering and *ab initio* molecular dynamics simulations confirm that the superionic Ag^+ ions are confined to sub-nanometre sheets, with the simulated local structure validated by experimental X-ray powder pair-distribution-function analysis. Finally, we demonstrate that the phase transition temperature can be controlled by chemical substitution of the alkali metal ions that comprise the immobile charge-balancing layers. Our work thus extends the known classes of SICs and will facilitate the design of new materials with tailored ionic conductivities and phase transitions.

Introduction

Superionic conductors (SICs) are solids which host liquid-like ionic conductivity, i.e., a diffusion coefficient, D of order $\sim 10^{-5}$ cm^2 s^{-1}, comparable to that of water at room temperature.[1] In addition to

1

attracting long-standing scientific interest,[2,3] this rapid ionic diffusion naturally lends itself to wide application in energy storage.[4,5] Recently, SICs have found utility in thermoelectric energy conversion, as atomic disorder and anharmonicity are linked to low lattice thermal conductivity[6,7] and hence, high thermoelectric efficiency.[8]

SICs generally undergo an order-disorder transition to the superionic state, and can be grouped into three classes by the nature of the transition.[1,9] Type I SICs exhibit an abrupt transition to the superionic state (e.g., AgI, Ag_2Se, *etc.*),[10] which becomes less well-defined for type II (continuous transition, e.g., PbF_2, $AgCrSe_2$),[11,12] and non-existent in the case of type III SICs (e.g., the β-aluminas).[13] In the superionic state, a non-conducting sublattice remains. This rigid network dictates the available conduction pathways and can be linked in one, two or three dimensions. Two-dimensional SICs, where long-range superionic diffusion is confined between immobile layers and ionic conduction is strongly anisotropic, are well represented in types II and III, such as $AgCrSe_2$[14] and Ag:β-Al_2O_3[15] respectively. In both of these types, the underlying layered structures are unchanged at the onset of fast ionic conduction and existing additional atomic sites become increasingly populated with increased temperature. Conversely, the type I SICs known to date have exclusively 3D crystal structures (cubic or hexagonal, cf Table 3.2, ref 1),[1] with the archetypical AgI undergoing a first-order superionic phase transition from an ordered, low symmetry phase to a body-centered cubic (bcc) arrangement of I^- ions (α-AgI) with significant Ag^+ ion disorder at 420 K.[16] Similarly, orthorhombic β-Ag_2Se transforms to the bcc superionic phase, α-Ag_2Se at 406 K.[17]

Previously, we identified a first order, order-disorder phase transition in 2D KAg_3Se_2 – a dimensionally-reduced derivative of 3D Ag_2Se – at ~695 K using in-situ X-ray diffraction and differential scanning calorimetry (Figure S1 in the Supporting Information (SI)).[18] However, the elevated temperature of the transition prevented measurement of the ionic conductivity because of reactions between KAg_3Se_2 and the electrode materials. Here, we use quasi-elastic neutron scattering (QENS) and complementary *ab initio* molecular dynamics (AIMD) simulations to reveal that the

high temperature phase, α-KAg$_3$Se$_2$, is a superionic Ag$^+$ ion conductor, with the quasi-molten Ag sublattice restricted to 4 Å thick layers. To the best of our knowledge, this represents the first type I superionic conductor with a 2D structure. Progressive reduction of long-range order through the melting point was probed by X-ray total scattering measurements, and the superionic local structure is also in good agreement with the AIMD simulations.

Chemical substitution has been an important tool in the design and modification of SICs; the most famous example being RbAg$_4$I$_5$, where substitution of Rb for Ag in AgI resulted in the highest room temperature solid-state ionic conductivity to date.[19] To investigate these effects we synthesized a series of cation-substituted AAg$_3$Se$_2$ (A = Li-Cs) compounds. Thermal analyses indicate that the superionic transition temperature can be tuned by the composition of alkali metal ions within the immobile layers.

Results

Quasi-Elastic Neutron Scattering (QENS). QENS probes small energy transfers around a central elastic scattering peak. Dynamic processes, such as diffusion, manifest as peak broadening that grows at the expense of elastic intensity.[20] The Q-dependence of this broadening yields information on these processes, with a linear dependence on Q^2 being indicative of translational diffusion following Fick's second law.[21]

Elastic scans acquired on heating from 300 to 740 K showed a sharp decrease in elastic intensity at ~680 K (Figure S2 in the SI), concurrent with the β-α phase transition previously reported,[18] and the on-set of quasi-elastic (QE) scattering (Figure 1a). The spectra collected of the can containing only empty fused-silica tubes overlapped with the elastic peak observed at room temperature (Figure 1b) – therefore the quasi-elastic component was from the sample only. These data were fit using delta, linear background and Lorentzian functions (Figure 1c and Section S1 in the SI), where the delta function represented purely elastic scattering and a single Lorentzian function captured the QE

scattering component. The half-width half-maximum of this peak, Γ was plotted as a function of Q^2 to yield information on diffusing species in the sample.

These QE scattering data were well-described by a linear fit through the origin, indicating translational Fickian diffusion in the superionic phase (see Figure 1d and Figure S3 in the SI). Similar QENS results were observed in α-Ag$_2$Se, where simple Fickian diffusion was also assigned.[22] In more complex jump-diffusion models, *e.g.*, the Chudley-Elliot model,[23] oscillatory behavior of Γ occurs with increasing Q^2, associated with discrete jumps on a crystalline sublattice. Although the limited Q-range here means we cannot comment on the applicability of more complex models, this should not significantly affect the magnitude of the diffusion coefficient.[24] The diffusion coefficient, D determined from this analysis was approximately 10^{-5} cm^2 s^{-1} from 710 to 740 K, corresponding to superionic diffusion in α-KAg$_3$Se$_2$. Additional QE scattering data were collected below the transition, at 600 and 650 K, but did not exhibit features consistent with long-range diffusion (Section S1 and Figure S4 in the SI).

Interpretation of QENS data is straightforward in the case of incoherent scattering, which pertains to single particle dynamics and hence, directly to diffusion.[21] Ag primarily scatters neutrons coherently, with the coherent scattering cross-section being roughly an order of magnitude larger than that of the incoherent contribution (4.41 and 0.58 barns respectively).[25] To account for coherency effects, the structure factor, $S(Q)$ should be considered when modelling $\Gamma(Q)$.[26] However, in QENS studies of superionic α-Ag$_2$Se, coherency effects were found to be negligible for $Q^2 < 2$ Å^{-2} (the maximum Q^2 value in our experiments), and the extracted diffusion coefficient from DQ^2 analysis matched values from ionic conductivity measurements and AIMD simulations.[22] Similarly, incoherent QENS analysis of the Cu$^+$-ion SICs (Cu also mainly scatters neutrons coherently), α-Cu$_2$Se[6] and a-CuCrSe$_2$[27] yielded diffusion coefficient values in good agreement with conductivity measurements and molecular dynamics simulations – again suggesting minimal coherency effects. Therefore, our

approach is reasonable based on previous results and the agreement between our incoherent DQ^2 analysis and complementary AIMD simulations.

***Ab initio* Molecular Dynamics (AIMD) Simulations.** Molecular dynamics simulations were performed to gain insights into the superionic behavior of KAg_3Se_2. Simulations of the low temperature β-KAg_3Se_2 phase showed no diffusion at 300 K, but larger displacements for Ag atoms (Figure S5a in the SI), consistent with the single-crystal structure solution.[28] Additional simulations at 600 and 650 K showed no long-range diffusion of Ag^+-ions in the β-phase (Figure S5b and c in the SI), consistent with the corresponding QENS experiments at these temperatures. As shown in Figure 2a, simulations of the superionic α-phase (space group *R-3m,* #166) displayed superionic Ag^+ diffusion on the order of 10^{-5} cm^2 s^{-1} at 800 K, in excellent agreement with the QENS analysis. In contrast, K and Se did not show characteristics of diffusion and so comprise the rigid sublattice in α-KAg_3Se_2. Mobile Ag^+ ions are therefore sandwiched between $[KSe_2]^{3-}$ slabs of edge-sharing KSe_6 octahedra (see Video S1 in the SI). This quasi-2D confinement is unique in the category of type I SICs. Significant similarities exist between α-KAg_3Se_2 and other 2D Ag^+-ion SICs; especially with $AgCrSe_2$ (type II) which shares the *R-3m* space group and Se anion network, but also with Ag:β-Al_2O_3 (type III) which exhibits a hexagonal (*P6$_3$/mmc* space group, #194) crystal structure (Figure 2b). Although we note the difference between Ag:β-Al_2O_3, where conduction sites all lie within the same plane, and the conduction bi-layers present in α-KAg_3Se_2 and α-$AgCrSe_2$, here we define 2D SICs as those where long-range ionic diffusion is strongly anisotropic, i.e., there is negligible ionic conductivity perpendicular to the layers.

Additional AIMD simulations were performed at 700 and 900 K to obtain data points for activation energy analysis (Figure S6 in the SI). Simple fitting of D as a function of temperature was performed using an Arrhenius relationship,

$$D(T) = D_0 \exp(-E_a/k_B T), \qquad (1)$$

where, D_0 is a model-dependent pre-exponential factor, E_a is the activation energy for diffusion, k_B is the Boltzmann constant and T is temperature. Application of equation (1) yielded an $E_{a,AIMD} = 0.013(2)$ eV and $D_{0,AIMD} = 3.47(1) \times 10^{-5}$ cm^2 s^{-1}. The small E_a value, on the order of $k_B T$, was consistent with facile ionic diffusion and that measured for 3D type I SICs such as AgI,[29] Ag_2S[30] and Ag_2Se.[31,32] The experimental QENS data are consistent with the trend over the wider T range from simulations (Figure 2c).

Pair-Distribution-Function Analysis. Analyses of the local structures of the β, α and liquid phases of KAg_3Se_2 were achieved using X-ray pair-distribution-function (PDF) analysis. In the superionic α-phase, atomic correlations were broader and weaker in magnitude than in the ordered β-phase (Figure 3a). Liquid KAg_3Se_2 closely resembled the nearest-neighbor Ag-Se, Se-Se and Ag-Ag correlations in liquid Ag_2Se.[33]

The local structures of both β- and α-KAg_3Se_2 were well-described using the previously reported average structures and refining anisotropic atomic displacement parameters (ADPs). Weighted residuals (R_w) of ~10% and ~20% were achieved in the ordered β- phase and disordered α-phase respectively (Figure S7 in the SI). Full fitting details can be located in Section S2 in the SI. PDF analysis has been shown to produce reliable ADPs, comparable to those from single-crystal refinement.[34] Indeed, for the low temperature phase, the anisotropic ADPs were in good agreement with those from single-crystal data (Figure S8 in the SI). Three unique Ag atoms describe the corrugated $[Ag_3Se_2]^-$ layers, with Ag1 and Ag3 forming tunnels along the b-axis, which are bridged by Ag2 (Figure 3b). The type I superionic phase transition was observed around 700 K, fully occurring in a ~15 K window (Figure S9 in the SI). As shown in Figure 3b, the Ag ADPs became very large (all with U_{eq} of ~0.1 Å^2) and anisotropic as the transition was approached, consistent with the vibrations of these atoms, in particular Ag2, destabilising the ordered phase and driving the transition to the superionic state (see Section S2 in the SI).

In superionic a-KAg$_3$Se$_2$, the silver layers are comprised of two unique sites with 75% occupancy: Ag1 in a bent trigonal planar and Ag2 in a distorted tetrahedral coordination (Figure 3b). Both Ag sites are characterized by large displacement parameters which can indicate static or dynamic disorder. As shown in Figure 3c, the Ag probability densities derived from AIMD simulations qualitatively match the ADPs from PDF analysis, suggesting that the Ag ions are dynamically disordered – a common feature of SICs. Our simulations indicated no strong preference between Ag1 or Ag2 sites on the timescales probed here and that all Ag$^+$ ions were mobile, thus an in-plane ionic conductivity, $\sigma_I = neDZ/k_BT$, of ~0.5 S cm^{-1} could be estimated at 800 K. In contrast, probability distributions for K and Se showed localised and isotropic distributions, reflecting harmonic potentials (Figure S11 in the SI).

Cation Substitution. As shown in the preceding section, strongly anisotropic Ag thermal motion appears to drive the superionic transition with seemingly little contribution from the charge-balancing K-Se layers. Substitutions of K$^+$ with Na$^+$, Rb$^+$ and Cs$^+$ in the ordered β-phase of KAg$_3$Se$_2$ were accomplished by solid-state methods and the solid-transition onset temperatures, T_{solid}, were monitored using DTA (Figures 4 and S12 in the SI). Attempts at full replacement of K$^+$ with Li$^+$ or Na$^+$ ions resulted in no ternary formation or a new, unknown ternary phase respectively (see Figure S14 in the SI), while neither RbAg$_3$Se$_2$ nor CsAg$_3$Se$_2$ exhibited features consistent with a solid phase transition before melting (Figure 4a).

The lack of sharp transitions in the latter compounds was somewhat unexpected. Both RbAg$_3$Se$_2$ and CsAg$_3$Se$_2$ are isostructural with β-KAg$_3$Se$_2$, with virtually no change in Ag-Se interatomic distances (< 0.01 Å),[28] suggesting the underlying mechanism is not simply due to "chemical pressure" effects. To explore this further, a series of samples with compositions, A_xK$_{1-x}$Ag$_3$Se$_2$ (A = Na, Rb) were synthesized and characterised. A complete solid-solution was possible between KAg$_3$Se$_2$ and RbAg$_3$Se$_2$, while Na$_x$K$_{1-x}$Ag$_3$Se$_2$ was limited to x = 0.1, above which significant impurities were observed by PXRD (Figure S15 in the SI). Alternative synthetic approaches such as ion exchange,

flux or thin-film synthesis may be successful in realising compounds with increased Na content. The T_{solid} values for these series are shown in Figure 4b. When smaller ions were substituted for K, the T_{solid} decreased and the hysteresis between transitions on heating (endothermic) and cooling (exothermic) increased. Conversely, when Rb replaced K in the immobile, charge-balancing layers, the solid transition was pushed to higher temperatures with negligible hysteresis for members with $x \geq 0.25$. Comparing the T_{solid} values of the most Na-rich and Rb-rich compounds synthesised, chemical control of the solid transition of over 100 K is demonstrated. Taken altogether, we speculate that the larger alkali metal ions are less able to adopt the perfect octahedral geometry with Se observed in α-KAg_3Se_2 (Figures 2b and 3c), inhibiting the superionic transition and vice versa. This approach to modulating the superionic transition temperature is distinct from the nanoparticle size effects observed in AgI[35] or the effects of applied pressure and can be readily explored in bulk materials. However, further characterisation (e.g., in-situ X-ray ray scattering, differential scanning calorimetry, QENS) of additional members of these solid solutions $A_xK_{1-x}Ag_3Se_2$, where A = alkali metals will be required to definitively establish this trend and will be the focus of future work.

Conclusions

α-KAg_3Se_2 is a new type I superionic conductor and the first with a 2D crystal structure. Quasi-elastic neutron scattering (QENS) between 710 and 740 K yields a diffusion coefficient of $\sim 10^{-5}$ cm^2 s^{-1}, comparable to that of liquid water at room temperature. Our *ab initio* molecular dynamics (AIMD) simulations show that K and Se atoms form the immobile sublattice and the superionic Ag^+ ions reside in 4 Å thick infinite slabs. The AIMD simulations reproduce the diffusion coefficient from QENS and the local structure measured by powder X-ray pair-distribution-function analysis. Initial exploration of isostructural analogues suggests that, rather than any chemical pressure effects on the Ag-Se network, the malleability of the charge-balancing ions facilitates or inhibits the superionic phase transition temperature. The availability of this compound opens a new stage for experimentation aimed at studying in detail ionic motion confined in two dimensions. Our work

extends the known classes of superionic conductors and should facilitate the design of new materials with tailored ionic conductivities and phase transitions.

Methods

Reagents. The following reagents were used as received: sodium metal (99.9%, Sigma-Aldrich), potassium metal (99%, Sigma-Aldrich), rubidium metal (99%, Johnson Matthey) caesium metal (99.8%, Sigma-Aldrich), silver shot (99.99%, Alfa Aesar) and selenium shot (99.999%, Plasmaterials Inc.).

Synthesis. All chemical manipulations were conducted inside an Ar-filled glovebox (M-Braun) with oxygen and moisture levels < 0.1 ppm. Flame-sealing was performed by evacuating ampules to < 10^{-3} mbar. Phase-pure KAg_3Se_2 powder was synthesised directly from the elements, with K and Se physically separated by Ag shot to avoid a strongly exothermic reaction. Elemental ratios K:Ag:Se of 1.05:3:2 were used, with a 5% molar excess K to account for surface oxidation of the metal. In a typical experiment, K metal chunks (1.101 g, 28 mmol) were compacted in the bottom of an 18 mm O.D. (outer diameter) × 16 mm I.D. (inner diameter) fused-silica tube. Ag shot (8.682 g, 80 mmol) was then loaded followed by Se shot (4.237 g, 54 mmol) on top. To minimize the free volume inside the ampule, a 15 mm O.D. × 13 mm I.D. fused-silica tube was used as a snug-fitting plug above the elements. This assembly was then flame-sealed and placed upright in a box furnace. The mixture was heated to 400 °C in 12 h and held for 12 h after which the furnace was turned off.

A_2Se_3 (A = Rb, Cs) precursor powders were synthesized using a tube-in-tube method. Briefly, a stoichiometric amount of Se was suspended in an alumina crucible above Rb or Cs metal and flame-sealed in an 18 mm O.D. × 16 mm I.D. fused-silica tube while the bottom of the tube was submerged in liquid nitrogen. This assembly was placed upright in a muffle furnace and heated to 500 °C in 20 h and held at that temperature for 12 h before natural cooling to room temperature. A black A_2Se_3 ingot could be removed from the bottom of the tube in both cases. Li_2Se and Na_2Se were

9

produced by combining the elements in a 2:1 molar ratio in liquid ammonia using established procedures.[36]

To synthesise the $RbAg_3Se_2$ and $CsAg_3Se_2$ ternary compounds, A_2Se_3 (A = Rb, Cs), Ag and Se powders were homogenized in a mortar and pestle in a 1:6:1 molar ratio, loaded into a graphite crucible and capped with a graphite plug before being flame-sealed in a 15 mm O.D. × 13 mm I.D. fused-silica tube. These mixtures were heated to 400 °C in 3 h and held for 12 h before the furnace was turned off. Similar procedures were used for targeting $LiAg_3Se_2$, $Na_xK_{1-x}Ag_3Se_2$ (x = 0.05, 0.01, 0.25, 1) and $Rb_xK_{1-x}Ag_3Se_2$ (x = 0.05, 0.01, 0.25, 0.75) using stoichiometric molar ratios of Li_2Se, Na_2Se, Ag, Se, KAg_3Se_2 and $RbAg_3Se_2$. In all cases a black, homogeneous powder compact was produced. Powder X-ray diffractograms for all products can be located in the Supporting Information (SI, Figures S13 and 14).

Quasi-Elastic Neutron Scattering. Quasi-elastic neutron scattering (QENS) data were collected at the backscattering silicon spectrometer (BASIS)[37] at the Spallation Neutron Source, Oak Ridge National Laboratory (ORNL) using a Closed Cycle Refrigerator sample environment (maximum operating temperature: 740 K). Because of the high absorption cross-section of Ag, ~10 g of KAg_3Se_2 was loaded into four 7 mm O.D. × 6 mm I.D. fused-silica tubes and flame-sealed. These were placed side-by-side in the Al sample can to approximate a flat plate scattering geometry (see Figure S16 in the SI). Furnaces capable of higher temperature operation had much larger background scattering from Al and so were not suitable. First, short elastic scans from 300 to 740 K were measured. A change in elastic intensity around 680 K was assigned to the known order-disorder phase transition, albeit at a lower temperature than 695 K observed by differential scanning calorimetry (DSC). DSC measurements are thoroughly calibrated; thus, this discrepancy was attributed to poor sample-thermocouple coupling in the QENS sample environment. Spectra were then collected on cooling between 740 and 710 K in 10 K increments, followed by a long QENS measurements at 300 K, which was used as the instrument resolution function. Finally, four

nominally identical, empty, evacuated tubes were used for the background measurement at 740 K. Additional long QENS experiments were performed at 600 and 650 K. These data were collected on heating from room temperature to ensure the sample was in the β-phase. $S(Q,\omega)$ data were reduced using Mantid software[38] in the range -100 to 100 meV and binned in 0.04 meV steps over a Q range of 0.3-1.3 Å^{-1} binned in 0.1 Å^{-1} steps. Fitting of the QENS data (see Section S1 in SI) was performed using the Data Analysis and Visualization Environment (DAVE) package.[38] The bandwidth of incoming neutron was centered at 6.4 Å. Coherent scattering from Bragg peaks was present between $Q^2 = 0.5\text{-}0.64$ Å^{-2} and $Q^2 > 1.9$ Å^{-2}, thus these Q-ranges were excluded from the analysis (Figure S14 in the SI).[20] However, we note that the inclusion of these data did not markedly affect the fitting results.

Ab initio Molecular Dynamics Calculations. *Ab initio* molecular dynamics (AIMD) simulations were performed using the Vienna Ab initio Simulation Package (VASP),[39-41] using as exchange-correlation functional the generalized gradient approximation (GGA) in the Perdew-Burke-Ernzerhof (PBE) form.[42,43] Convergence tests were conducted with low temperature β-KAg$_3$Se$_2$, where a plane-wave cut-off energy of 350 eV and an electronic k-point mesh of $3 \times 12 \times 6$ were used. The electronic self-consistent loop converged to 10^{-8} eV and the forces were smaller than 10^{-4} eV/Å on all atoms. AIMD simulations were performed on a $4 \times 4 \times 1$ supercell of the superionic α-KAg$_3$Se$_2$ (288 atoms) using the experimental lattice constants, $a = 4.56$ Å, and c $= 25.41$ Å, with the Brillouin zone center, G, as the only k-point. Three parallel trajectories starting with random initial structures were calculated at 700, 800, and 900 K, and averaged for mean square displacement MSD calculations. For each initial structure, the stoichiometry (75% Ag site occupancy) was maintained by randomly removing 25% of Ag atoms in each layer. Additional simulations at 300, 600 and 650 K were conducted for the β-phase. Each trajectory was at least 55 ps long with 2 fs steps, and the first 5 ps were treated as equilibration time. Extraction of the diffusion coefficient was performed by linear fitting between the bounds of $0.5a^2$, where a is the jump distance, (~4.5 A^2) and 70% of the simulation time (35 ps) as recommended by He et al.[44]

Synchrotron X-ray Scattering. In-situ X-ray total scattering data were collected on heating at Sector 17-BM-B at the Advanced Photon Source from 300 to 950 K using a PerkinElmer amorphous silicon flat panel detector. KAg_3Se_2 powder was sieved to < 45 μm and loaded into a 0.3 mm diameter fused-silica capillary and flame-sealed. The sample was spun during collection and the wavelength used was 0.24141 Å. Integration and background subtraction was performed using GSAS-II software (version 3667),[45] transformation from $S(Q)$ to $G(r)$ using PDFgetX3[46] (with Q_{max} = 18 $Å^{-1}$) and fitting using pdfgui software.[47]

Powder X-ray Diffraction. Phase purity was determined by powder X-ray diffraction (PXRD). Data were collected using a Rigaku Miniflex diffractometer with a Ni-filtered Cu Ka source operating at 15 mA and 40 kV. Continuous scanning was utilized with a step size of 0.015°. Materials were finely ground and uniformly coated on a flat plate sample holder and protected from ambient conditions using Kapton film and vacuum grease.

Differential Thermal Analysis. Differential thermal analyses (DTA) were carried out using a Shimadzu DTA-50 thermal analyser. The powder samples (~30 mg total mass) were evacuated and sealed in carbon-coated, fused-silica ampules. A fused-silica ampule containing alumina powder was used as a reference. All samples were heated to the desired temperature at 5 K min^{-1}, followed by cooling at the same rate to 343 K. Transition temperatures were determined from the onset of endothermic or exothermic features.

Author Contributions

A.R., S.R. and M.G.K. conceived the study. A.R., X.Z. and D.-Y.C. synthesised and characterised all materials. A.R., R.O. and N.O. acquired and analysed neutron scattering data. J.D. and O.D. performed AIMD simulations. M.J. and C.M. conducted PDF analysis and structural modelling. The manuscript was mainly written and revised by A.R., S.R. and M.G.K. All authors approved the final version of the manuscript.

Competing Interests Statement

The authors declare no competing interests.

Associated Content

Supplementary Information

Experimental details of QENS measurements, additional AIMD simulations, PDF analysis, powder XRD of AAg_3Se_2 (A = Li-Cs) compounds and DTA data.

References

1   Boyce, J. B. & Huberman, B. A. Superionic conductors: Transitions, structures, dynamics. *Phys. Rep.* **51**, 189-265 (1979).
2   Faraday, M. VII. Experimental researches in electricity. *Phil. Trans. R. Soc* **128**, 83-123 (1838).
3   Hull, S. Superionics: crystal structures and conduction processes. *Rep. Prog. Phys* **67**, 1233-1314 (2004).

4   Goodenough, J. B. Review Lecture-Fast ionic conduction in solid. *Proc. R. Soc. A* **393**, 215-234 (1984).

5   Bruce, P. G. *Solid State Electrochemistry*. (Cambridge University Press, 1997).

6   Voneshen, D., Walker, H., Refson, K. & Goff, J. Hopping time scales and the phonon-liquid electron-crystal picture in thermoelectric copper selenide. *Phys. Rev. Lett.* **118**, 145901 (2017).

7   Ding, J. *et al.* Anharmonic lattice dynamics and superionic transition in $AgCrSe_2$. *Proc. Natl. Acad. Sci USA* **117**, 3930-3937 (2020).

8   Bailey, T. P. & Uher, C. Potential for superionic conductors in thermoelectric applications. *Curr. Opin. Green Sustainable Chem* **4**, 58-63 (2017).

9   Keen, D. A. Disordering phenomena in superionic conductors. *J. Condens. Matter Phys.* **14**, R819 (2002).

10   Funke, K. AgI-type solid electrolytes. *Prog. Solid. State Ch.* **11**, 345-402 (1976).

11   Derrington, C. & O'Keeffe, M. Anion conductivity and disorder in lead fluoride. *Nat. Phys. Sci.* **246**, 44-46 (1973).

12   Boukamp, B. & Wiegers, G. Ionic and electronic processes in $AgCrSe_2$. *Solid State Ion.* **9**, 1193-1196 (1983).

13   Yao, Y.-F. Y. & Kummer, J. Ion exchange properties of and rates of ionic diffusion in beta-alumina. *J. Inorg. Nucl. Chem.* **29**, 2453IN12467-24662475 (1967).

14   Engelsman, F., Wiegers, G., Jellinek, F. & Van Laar, B. Crystal structures and magnetic structures of some metal (I) chromium (III) sulfides and selenides. *J. Solid State Chem.* **6**, 574-582 (1973).

15   Newsam, J. & Cheetham, A. Stoichiometric silver beta alumina studied at 25, 300 and 500 degrees C by powder neutron diffraction. *J. Phys. Condens. Matter* **2**, 2335 (1990).

16   Tubandt, C. & Lorenz, E. Molekularzustand und elektrisches Leitvermögen kristallisierter Salze. *Z. Phys. Chem* **87**, 513-542 (1914).

17   Miyatani, S.-y. Ionic conductivity in silver chalcogenides. *J. Phys. Soc. Jpn* **50**, 3415-3418 (1981).

18   Rettie, A. J. E. *et al.* Ag_2Se to KAg_3Se_2: Suppressing Order–Disorder Transitions via Reduced Dimensionality. *J. Am. Chem. Soc.* **140**, 9193-9202 (2018).

19   Raleigh, D. O. Ionic conductivity of single-crystal and polycrystalline $RbAg_4I_5$. *J. Appl. Phys.* **41**, 1876-1877 (1970).

20   Mamontov, E. Fast oxygen diffusion in bismuth oxide probed by quasielastic neutron scattering. *Solid State Ion.* **296**, 158-162 (2016).

21   Bée, M. Localized and long-range diffusion in condensed matter: state of the art of QENS studies and future prospects. *Chem. Phys.* **292**, 121-141 (2003).

22   Hamilton, M., Barnes, A., Howells, W. & Fischer, H. Ag^+ dynamics in the superionic and liquid phases of Ag_2Se and Ag_2Te by coherent quasi-elastic neutron scattering. *J. Phys. Condens. Matter* **13**, 2425 (2001).

23   Chudley, C. & Elliott, R. Neutron scattering from a liquid on a jump diffusion model. *Proc. Phys. Soc.* **77**, 353 (1961).

24   Embs, J. P., Juranyi, F. & Hempelmann, R. Introduction to quasielastic neutron scattering. *Z. Phys. Chem* **224**, 5-32 (2010).

25   Hempelmann, R. *Quasielastic neutron scattering and solid state diffusion*. (Clarendon Press, 2000).

26   Wind, J., Mole, R. A., Yu, D. & Ling, C. D. Liquid-like ionic diffusion in solid bismuth oxide revealed by coherent quasielastic neutron scattering. *Chem. Mater.* **29**, 7408-7415 (2017).

27   Delaire, O. *et al.* Selective breakdown of phonon quasiparticles across superionic transition in CuCrSe 2. *APS* **2019**, R47. 002 (2019).

28   Bensch, W. & Dürichen, P. Crystal structure of potassium diselenotriargentate, KAg_3Se_2. *Z. Kristallogr. - New Cryst. Struct.* **212**, 97-98 (1997).

29   Kvist, A. & Josefson, A.-M. The electrical conductivity of solid and molten silver iodide. *Z. Naturforsch. A* **23**, 625-626 (1968).

30 Allen, R. L. & Moore, W. J. Diffusion of silver in silver sulfide. *J. Phys. Chem.* **63**, 223-226 (1959).

31 Okazaki, H. Deviation from the Einstein relation in average crystals self-diffusion of Ag^+ ions in α-Ag_2S and α-Ag_2Se. *J. Phys. Soc. Jpn* **23**, 355-360 (1967).

32 Rom, I. & Sitte, W. Composition dependent ionic and electronic conductivities and chemical diffusion coefficient of silver selenide at 160 C. *Solid State Ion.* **101**, 381-386 (1997).

33 Barnes, A., Lague, S., Salmon, P. & Fischer, H. A determination of the structure of liquid Ag_2Se using neutron diffraction and isotopic substitution. *J. Phys. Condens. Matter* **9**, 6159 (1997).

34 Lee, S. & Xu, H. Using complementary methods of synchrotron radiation powder diffraction and pair distribution function to refine crystal structures with high quality parameters—A Review. *Minerals* **10**, 124 (2020).

35 Makiura, R. *et al.* Size-controlled stabilization of the superionic phase to room temperature in polymer-coated AgI nanoparticles. *Nat. Mater.* **8**, 476-480 (2009).

36 Sharp, K. W. & Koehler, W. H. Synthesis and characterization of sodium polyselenides in liquid ammonia solution. *Inorg. Chem.* **16**, 2258-2265 (1977).

37 Mamontov, E. & Herwig, K. W. A time-of-flight backscattering spectrometer at the Spallation Neutron Source, BASIS. *Rev. Sci. Instrum.* **82**, 085109 (2011).

38 Arnold, O. *et al.* Mantid—Data analysis and visualization package for neutron scattering and μ SR experiments. *Nucl. Instrum. Methods Phys. Res. A* **764**, 156-166 (2014).

39 Kresse, G. & Furthmüller, J. Efficient iterative schemes for ab initio total-energy calculations using a plane-wave basis set. *Phys. Rev. B* **54**, 11169 (1996).

40 Kresse, G. & Furthmüller, J. Efficiency of ab-initio total energy calculations for metals and semiconductors using a plane-wave basis set. *Comput. Mater. Sci.* **6**, 15-50 (1996).

41 Kresse, G. & Hafner, J. Ab initio molecular dynamics for liquid metals. *Phys. Rev. B* **47**, 558 (1993).

42 Perdew, J. P., Burke, K. & Ernzerhof, M. Generalized gradient approximation made simple. *Phys. Rev. Lett.* **77**, 3865-3868 (1996).

43 Perdew, J. P. & Zunger, A. Self-interaction correction to density-functional approximations for many-electron systems. *Phys. Rev. B* **23**, 5048 (1981).

44 He, X., Zhu, Y., Epstein, A. & Mo, Y. Statistical variances of diffusional properties from ab initio molecular dynamics simulations. *Npj Computational Materials* **4**, 1-9 (2018).

45 Toby, B. H. & Von Dreele, R. B. GSAS-II: the genesis of a modern open-source all purpose crystallography software package. *J. Appl. Crystallogr.* **46**, 544-549 (2013).

46 Juhás, P., Davis, T., Farrow, C. L. & Billinge, S. J. L. PDFgetX3: a rapid and highly automatable program for processing powder diffraction data into total scattering pair distribution functions. *J. Appl. Crystallogr.* **46**, 560-566 (2013).

47 Farrow, C. L. *et al.* PDFfit2 and PDFgui: computer programs for studying nanostructure in crystals. *J. Phys. Condens. Matter* **19**, 335219 (2007).
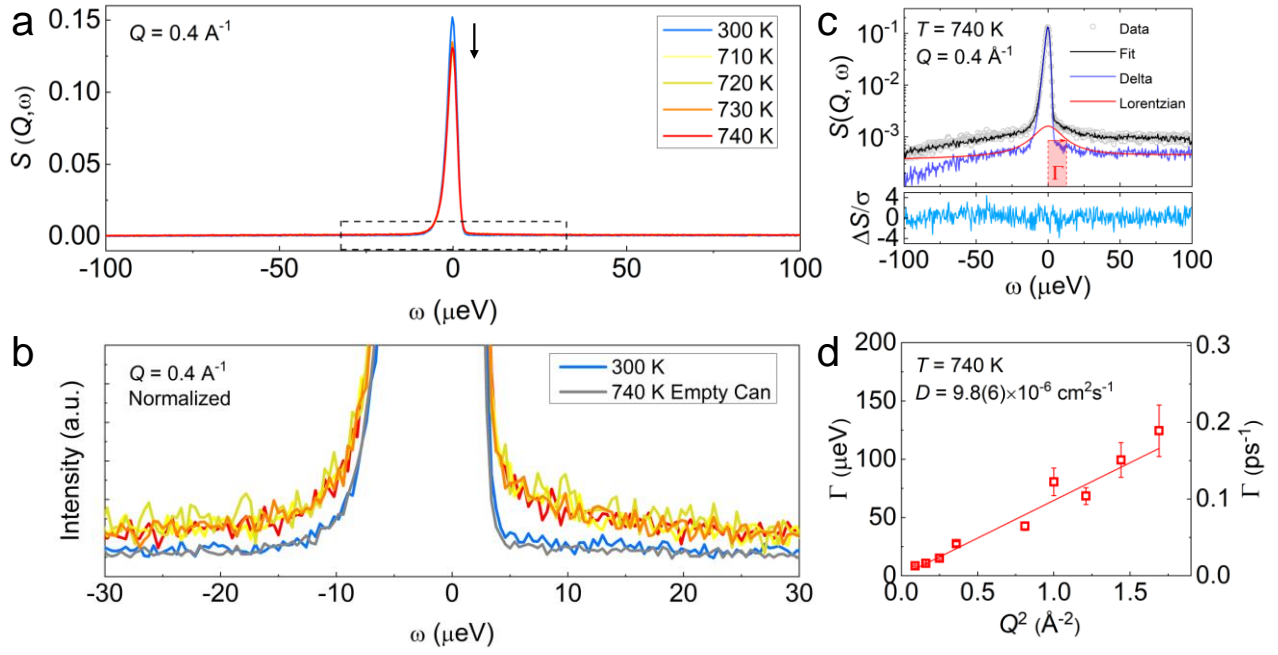
Figures and Captions

Figure 1. a) Representative QENS spectra at $Q = 0.4$ Å^{-1} as a function of temperature for KAg$_3$Se$_2$. The arrow shows a sharp decrease in elastic intensity for the high temperature α-phase. **b)** Normalised $S(Q,\omega)$ from the boxed region in b), illustrating quasi-elastic broadening in α-KAg$_3$Se$_2$. The legend is the same as A). **c)** Fitting of $S(Q,\omega)$ at 740 K and $Q = 0.4$ Å^{-1} using linear background (BG), delta and Lorentzian functions. Note that the BG function has been added to the Lorentzian component for clarity. **d)** Half-width half-maximum of the Lorentzian component, Γ vs. Q^2. A linear fit yielded the diffusion coefficient, D. Q-regions that include strong Bragg contributions have been omitted.
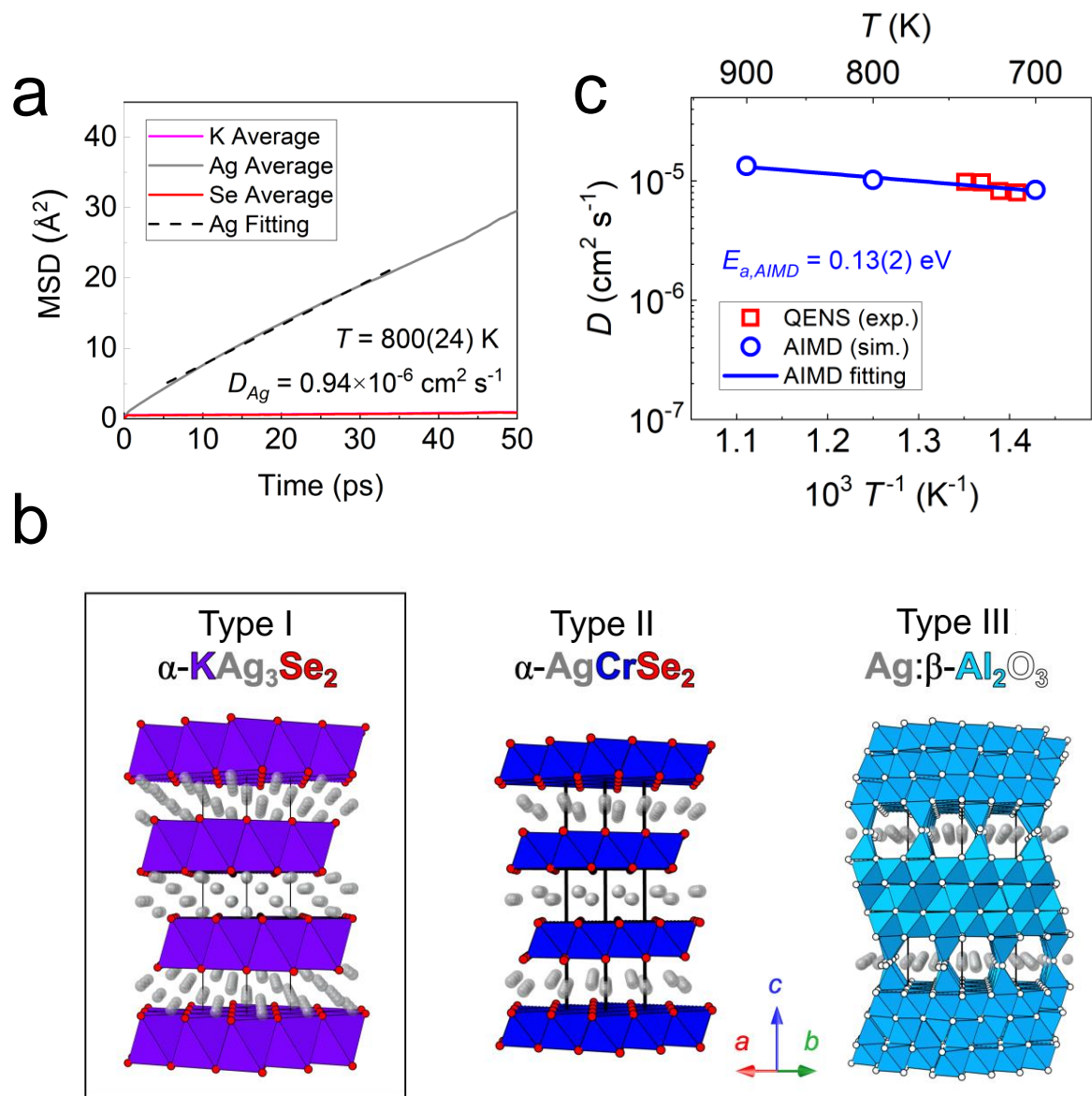
Figure 2. a) AIMD simulated mean square displacement (MSD) of atomic species in α-KAg$_3$Se$_2$ at 800 K. The linear fit yields the diffusion coefficient of Ag ions. **b)** Crystal structures of 2D Ag$^+$ ion SICs organized by type. The immobile rigid lattice is represented by solid polyhedra and the mobile Ag$^+$ ions as translucent spheres. The unit cells are drawn with solid black lines. **c)** Extracted diffusion coefficients from QENS (open red squares) and those derived from AIMD simulations (open blue circles) vs. reciprocal temperature. Error bars have been omitted for clarity but were used in the determination of the AIMD activation energy (linear fit represented by a solid blue line).
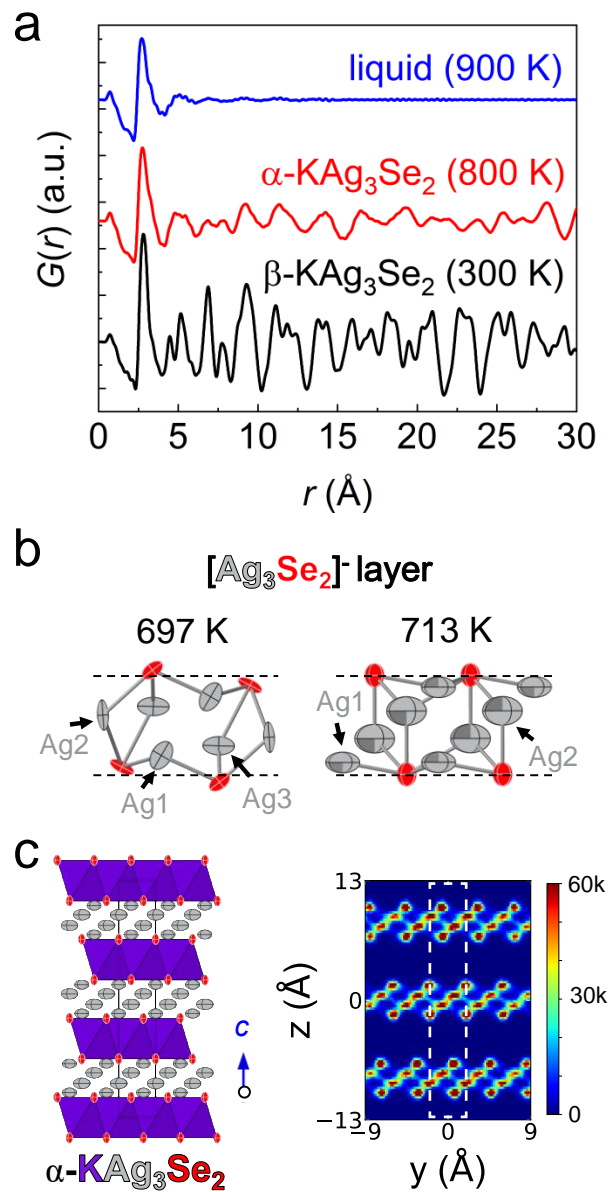
Figure 3. a) In-situ X-ray PDF of KAg$_3$Se$_2$ powder. **b)** Refined local structures of the Ag-Se layers just below (697 K) and just above (713 K) the superionic transition, in the β- and α-phases respectively. Note that the Ag atoms at 713 K (α-phase) have 75% occupancy. **c)** Crystal structure of α-KAg$_3$Se$_2$ from PDF analysis (left) compared with simulated Ag probability densities, both at 800 K (right). The unit cell is shown by solid black and dashed white lines respectively. Thermal ellipsoids are shown at 50%.
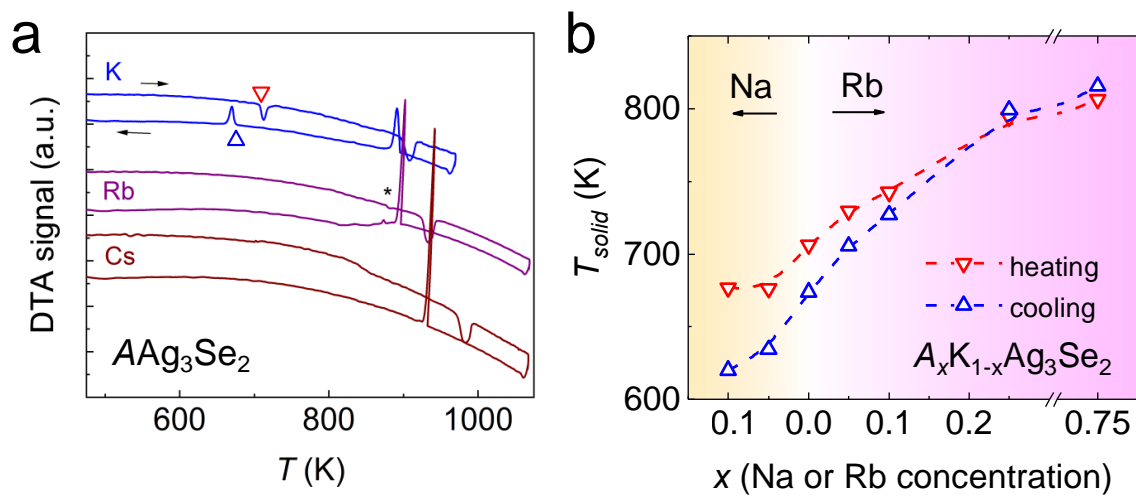
Figure 4. a) DTA curves for $A\text{Ag}_3\text{Se}_2$ (A = K-Cs) illustrating the effect of cation substitution on endo/exothermic (red down triangle/blue up triangle symbols respectively) features prior to melting/crystallisation at *ca.* 900 K. The DTA signal is not quantitative, *i.e.*, the signal depends on sample and reference masses as well as sample composition. Small unknown impurity peaks for the RbAg$_3$Se$_2$ trace are indicated with a "*"symbol. **b)** Solid transition onset temperatures from DTA on heating and cooling for $A_x\text{K}_{1-x}\text{Ag}_3\text{Se}_2$ (A = Na or Rb). DTA traces for all mixed-alkali compounds can be located in Figure S12 in the SI.